Dalton
Transactions

ROYAL SOCIETY
OF CHEMISTRY

PAPER

View Article Online
View Journal | View Issue

Published on 05 March 2026. Downloaded on 5/23/2026 5:05:50 AM.

Check for updates

Cite this: *Dalton Trans.*, 2026, **55**, 5168

An ultra-broadband and thermally tunable terahertz metamaterial absorber with high fabrication tolerance

Hao Shi,[a] Chunlan Wang,*[b] Tao Liu,[b] Lichao Yang,[b] Zekun Liu,[b] Xiaoming Mo *[a] and Yougen Yi *[c]

Received 16th January 2026,
Accepted 4th March 2026

DOI: 10.1039/d6dt00113k

rsc.li/dalton

Terahertz (THz) broadband absorbers with high efficiency and tunability are crucial for applications in electromagnetic shielding, sensing, stealth technology, and THz communication systems. In this work, an ultra-broadband, thermally tunable THz absorber with high fabrication tolerance is proposed based on the phase-change material vanadium dioxide (VO_2). The absorber adopts a metal–dielectric–metal (MDM) configuration, consisting of a gold reflective layer, a SiO_2 dielectric spacer, and a patterned VO_2 top layer. When VO_2 is in the metallic phase, the absorber achieves absorptance exceeding 90% over the frequency range of 3.1–10.0 THz, with a large fractional bandwidth of 105.34%. The broadband absorption mechanism is revealed through impedance matching analysis, multiple reflection interference theory, electric-field distribution analysis, and multipole decomposition. The results show that the absorption is primarily driven by electric dipole resonance, with contributions from toroidal and magnetic dipole resonances, which effectively confine electromagnetic energy and suppress reflection. Thermal modulation of the VO_2 phase transition enables dynamic tunability of the absorption response, while parametric and structural-shape analyses confirm excellent fabrication tolerance. This work demonstrates that the proposed VO_2-based metamaterial absorber provides a practical solution for advanced THz functional devices, combining high efficiency, broadband performance, and robust fabrication compatibility.

1. Introduction

Terahertz (THz) waves are electromagnetic waves that lie between microwaves and infrared radiation, with frequencies in the range of 0.1–10 THz.[1–3] These waves exhibit distinctive characteristics, such as a broad spectral range, high security, strong penetration, excellent interference resistance, and unique fingerprint spectra.[4,5] Due to these properties, THz waves have significant potential in a wide range of applications, particularly in ultra-high-speed communications, substance identification, biomedical investigations, and nondestructive testing.[6–8] As a result, the development of THz technology remains a focus of academic research. Despite the fact that research on THz devices garners widespread attention, THz waves have minimal interaction with natural materials. This situation presents substantial hurdles to their development. To overcome the weak interaction between THz waves and natural materials, researchers have developed metamaterials. Metamaterials are composite materials with periodic, subwavelength designs that exhibit significant responses to THz waves and can modulate the amplitude, phase, and polarization characteristics of electromagnetic waves, thereby contributing to breakthroughs in THz technology.[9,10] Currently, metamaterials are used in the design of various THz devices, such as absorbers, polarization converters, and superlenses.[11–14] Among them, metamaterial absorbers have gained widespread application in stealth coatings, electromagnetic shielding, THz thermal emitters, and sensors, owing to their strong energy dissipation and tunable resonant characteristics.[15–17]

The first metamaterial perfect absorber demonstrates the feasibility of metamaterials for absorber design. This milestone lays a solid foundation and provides a valuable reference for subsequent research.[18] Since then, extensive research efforts have been devoted to absorber development, and various THz metamaterial devices capable of achieving near-perfect absorption at specific THz frequencies have been reported. However, conventional metamaterial absorbers gradually reveal several

---

[a] *Center on Nanoenergy Research, Guangxi Key Laboratory for Relativistic Astrophysics, School of Physical Science and Technology, Guangxi University, Nanning, Guangxi, 530004, China. E-mail: xmmo@gxu.edu.cn*
[b] *School of Science, Xi'an Polytechnic University, Xi'an 710048, China. E-mail: wangchunlan@whu.edu.cn*
[c] *College of Physics, Central South University, Changsha 410083, China. E-mail: yougenyi@csu.edu.cn*

This journal is © The Royal Society of Chemistry 2026

Published on 05 March 2026. Downloaded on 5/23/2026 5:05:50 AM.

notable limitations. The most prominent issue is the fixed absorption characteristics and limited functionality, which prevent effective operation in complex and dynamic environments and make it difficult to meet the needs of researchers.[19,20] Therefore, introducing active materials into absorber design to achieve wide absorption bands, dynamically tunable absorption rates, structural simplicity, and broad applicability becomes an important research focus. Existing research suggests that three typical design strategies are widely used to achieve multi-peak or broadband absorption: the first is to adopt vertically coupled multilayer structures to enable multilevel resonance absorption through interlayer coupling,[21,22] the second is to use planar patterned metasurfaces with geometrically diversified unit cells to excite hybridized surface plasmon polaritons and intermodal coupling,[23,24] and the third is to develop hybrid photonic-crystal-based or plasma-assisted metastructures to realize broadband or asymmetric absorption–transmission responses.[25,26]

Various VO_2-based metamaterial perfect absorbers have recently been proposed. VO_2, as a typical phase-change material, exhibits thermally tunable properties with a critical transition temperature of approximately 341 K. During the phase transition, VO_2 can rapidly switch between insulating and metallic states, thereby enabling effective modulation of the absorption of incident electromagnetic waves.[27] Broadband THz absorbers based on patterned slotted VO_2 have been extensively investigated. Absorptance exceeding 90% is achieved over the frequency range of 1.5–4.2 THz, corresponding to an absorption bandwidth of 2.7 THz. By tuning the electrical conductivity of VO_2, the amplitude of the absorption peaks can be effectively modulated, with the absorptance varying from 2.5% to 99%.[28] In addition, THz metamaterial absorbers exhibiting switchable broadband and dual-narrowband absorption characteristics have been reported. Benefiting from the phase-transition properties of VO_2, dynamic switching functionality can be realized. In the metallic state, absorptance exceeding 90% is observed over the frequency range of 3.26–6.91 THz, corresponding to a bandwidth of 3.65 THz, whereas in the insulating state, two distinct absorption peaks appear at 1.72 THz and 4.96 THz, with peak absorptance reaching 99.3% and 99.9%, respectively.[29] Furthermore, dynamically tunable broadband THz absorbers demonstrate absorptance above 90% over the frequency range of 4.00–10.08 THz, with near-perfect absorption occurring in multiple subbands. The absorption level can be dynamically tuned from 1.2% to 99.9%.[30] More recently, VO_2-based tunable metamaterial absorbers achieved high absorptance exceeding 90% within the frequency range of 2.82–9.17 THz.[31]

The enhanced performance of VO_2-based absorbers mainly originates from two key factors. First, the large imaginary part of the permittivity of VO_2, together with its thermally controlled phase-transition behavior, contributes to strong dielectric losses, thereby significantly enhancing electromagnetic absorption.[32] Second, the patterned design induces localized electric-field enhancement and spatially inhomogeneous charge distributions.[33] These effects stimulate higher-order multipolar resonances, resulting in a broadened absorption bandwidth. Designing a THz absorber that not only provides a wider operational bandwidth but also maintains high fabrication tolerance poses a significant challenge for the development of multifunctional THz absorbers. Currently, some THz absorbers prioritize bandwidth enhancement at the expense of structural simplicity and fabrication robustness, which severely limits their feasibility for practical engineering applications.[34]

In this work, we propose an ultra-broadband, thermally tunable THz absorber with high fabrication tolerance, based on the phase-change material VO_2. The absorber adopts a metal–dielectric–metal (MDM) configuration, consisting of a metallic reflective layer, a SiO_2 dielectric spacer, and a patterned VO_2 top layer. Theoretical and simulation results indicate that when VO_2 is in the metallic phase, the device maintains absorption exceeding 90% over the frequency range of 3.1–10.0 THz, with a peak absorption of 97.4% and a fractional bandwidth of 105.34%. Using the impedance-matching principle, the multiple reflection interference model, electromagnetic field distribution analysis, and multipolar decomposition, it is demonstrated that the synergistic resonance between electric dipoles and toroidal dipoles gives rise to a hybrid absorption mode, which serves as the primary mechanism for broadband absorption. Furthermore, by varying the incident angle of the THz waves, temperature, structural parameters, and intermediate VO_2 patterns, the absorber is shown to exhibit tunable absorption characteristics, wide-angle absorption performance, and high fabrication tolerance. In summary, the proposed structure provides an effective and practical solution for applications in THz communications, radar stealth, intelligent switching, and electromagnetic shielding.

2. Design and method

Fig. 1 illustrates the schematic of the proposed THz absorber. As shown in Fig. 1(b), the unit cell of the designed device adopts a typical three-layer MDM configuration.[35] The top layer consists of a patterned VO_2 layer, as depicted in Fig. 1(c), which is composed of fourfold-symmetric fan-shaped structures and a central pattern. This specific geometrical design is capable of exciting localized surface plasmon resonances (LSPRs) within the central structure, while the narrow gaps between the fan-shaped segments and the central pattern further enhance the plasmonic resonance strength.[36,37] Consequently, perfect absorption can be achieved over a broader frequency band. The intermediate dielectric layer is composed of SiO_2, which can be regarded as an almost lossless dielectric material in the THz frequency range. This trilayer configuration is designed to enhance polarization stability and coupling strength. The bottom reflective layer consists of a gold film with a thickness of 2 μm, which is much larger than the skin depth of THz waves. As a result, the metallic layer does not participate in plasmonic resonance, and the transmission of the device is effectively suppressed to zero. It

Published on 05 March 2026. Downloaded on 5/23/2026 5:05:50 AM.

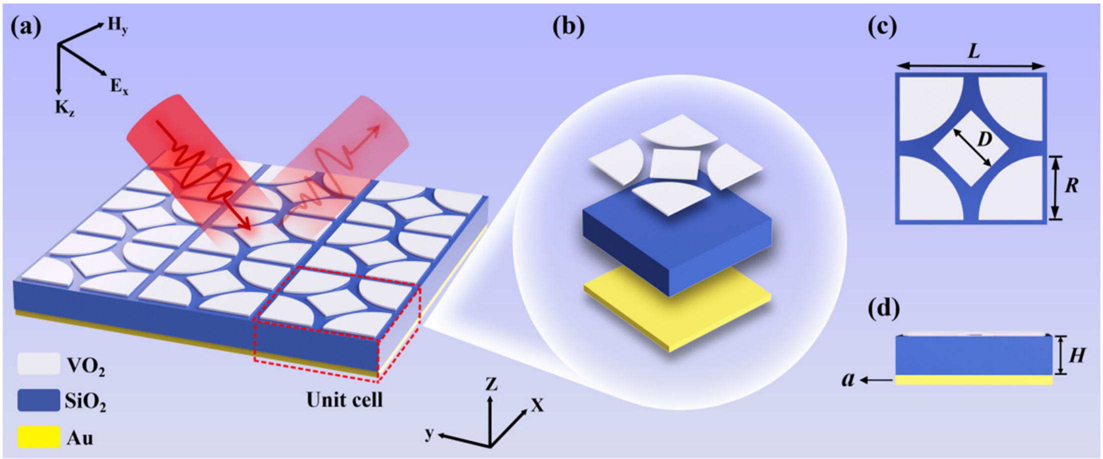

Fig. 1 Schematic diagram of the device structure: (a) Periodic structure diagram of the device, (b) 3D schematic of the unit cell, (c) Top view of the unit cell, (d) Side view of the unit cell.

should be emphasized that the electrical conductivity of gold is 4.09×10^7 S·m^{-1}. The gold layer serves to block electromagnetic transmission and generate total reflection, which is beneficial for destructive interference, thereby significantly enhancing electromagnetic energy localization and absorption efficiency.[38]

In this study, the absorption performance of the proposed device in the frequency range of 2–10 THz is modeled and numerically analyzed using the finite-element simulation software COMSOL Multiphysics.[39] Since the simulated structure represents a single unit cell, periodic boundary conditions need to be defined around the unit. Specifically, periodic boundary conditions are imposed along the x and y axis directions, and Floquet ports are configured at the incident boundaries to simulate an infinite periodic array.[40] Along the z-direction, perfectly matched layers (PMLs) are implemented, and normally incident plane waves with transverse electric (TE) and transverse magnetic (TM) polarizations are employed to simulate the electromagnetic response under free-space conditions.[41,42] During the meshing process, an adaptive mesh refinement strategy is adopted to balance computational accuracy and efficiency across the entire unit cell. Local mesh refinement is applied at metal edges and dielectric interfaces to ensure numerical convergence in regions with rapid electric-field variations. After systematic parameter optimization, the optimized structural parameters are determined as follows: fan-shaped radius R = 10 μm, side length of the central rhombus D = 10 μm, dielectric layer thickness H = 7.7 μm, gold reflector thickness a = 2 μm, and unit cell period L = 25 μm.

Considering the inherent fabrication tolerance of the proposed structure, a cost-effective magnetron sputtering technique can be primarily employed for device fabrication. A typical fabrication process can be summarized as follows.[43,44] First, a silicon substrate is ultrasonically cleaned sequentially in acetone, anhydrous ethanol, and deionized water. Subsequently, a 2 μm thick gold film is deposited onto the substrate by magnetron sputtering under a pure argon atmosphere. Next, a SiO_2 dielectric layer is deposited using plasma-enhanced chemical vapor deposition (PECVD). To continue the fabrication process, the SiO_2 target is replaced, and a 7.7 μm thick SiO_2 dielectric layer, with lateral dimensions of 25 μm, is then sputtered onto the gold layer. Following this, a thin VO_2 film is deposited onto the SiO_2 layer, forming a SiO_2/VO_2 stack for subsequent pattern definition. For the top-layer structure, arrays of patterned VO_2 can be generated by direct sputtering of the metal mask plate first, due to the good process tolerance of the multifunctional terahertz absorber that we have designed.

After completing the material deposition, a photoresist layer is spin-coated onto the surface, and electron-beam lithography (EBL) is employed to define the periodic array patterns. Following the lithography process, VO_2 is sputtered, and the excess photoresist is removed to form a patterned structure. Finally, the VO_2 film is patterned using inductively coupled plasma (ICP) etching to obtain the final device.[45]

VO_2 is a temperature-sensitive material whose phase state undergoes reversible transitions with temperature variation. At room temperature, VO_2 remains in an insulating state. As the temperature increases, charge carriers within the material are thermally activated, leading to a significant increase in electrical conductivity and a gradual transition from the insulating phase to the metallic phase.[28,29] In the THz frequency range, the relative permittivity of VO_2, in both the insulating and metallic states, can be described using the Drude model:[46]

$$\varepsilon_{VO_2} = \varepsilon_\infty - \frac{{\omega_p}^2}{\omega^2 + i\omega\gamma} \tag{1}$$

where ε_∞ = 12 represents the high-frequency dielectric constant, $\gamma = 5.75 \times 10^{13}$ rad·s^{-1} denotes the electron collision frequency, and ω is the angular frequency of the incident tera-

This journal is © The Royal Society of Chemistry 2026

Published on 05 March 2026. Downloaded on 5/23/2026 5:05:50 AM.

hertz wave. The plasma frequency $\omega_p{}^2(\sigma)$ of VO_2 is related to its conductivity by:[30,31]

$$\omega_p{}^2 = \frac{\sigma}{\sigma_0}\omega_p^2(\sigma) \tag{2}$$

where $\sigma_0 = 3 \times 10^5\ \mathrm{S{\cdot}m^{-1}}$ and $\omega_p(\sigma) = 1.4 \times 10^{15}\ \mathrm{rad{\cdot}s^{-1}}$. In this work, the electrical conductivity of VO_2 is set to $2 \times 10^2\ \mathrm{S{\cdot}m^{-1}}$ in the insulating state and $2 \times 10^5\ \mathrm{S{\cdot}m^{-1}}$ in the metallic state. Unless otherwise stated, VO_2 is described by the Drude model with conductivity values representing the insulating and metallic phases ($\sigma = 2 \times 10^2\ \mathrm{S{\cdot}m^{-1}}$ and $2 \times 10^5\ \mathrm{S{\cdot}m^{-1}}$, respectively), consistent with typical THz-range parameters reported for VO_2 across the insulator–metal transition. The Au ground plane is modeled as a good conductor using a frequency-independent conductivity $\sigma = 4.09 \times 10^7\ \mathrm{S{\cdot}m^{-1}}$. Given the 2 μm Au thickness is far larger than the THz skin depth, transmission is negligible and the absorption response is dominated by reflection suppression.[47,48]

3. Results and discussion

To elucidate the broadband absorption mechanism of the THz absorber, multiple reflection interference theory (MRIT) is introduced. Within this framework, the proposed structure can be regarded as an equivalent Fabry–Perot cavity. When THz waves impinge on the absorber (Fabry–Perot cavity), cumulative interference effects arise due to multiple reflections between the top metallic resonator and the bottom metallic ground plane, where destructive interference among the reflected waves leads to near-perfect absorption.[49,50] Fig. 2(a) schematically illustrates the interference-based mechanism. Here, R_{12} denotes the reflection at the top metallic resonator, T_{12} represents the transmission of the incident wave into the dielectric layer, R_{23} corresponds to the reflection at the bottom metallic plane, and T_{21} marks the transmission leaking out of the SiO_2 layer into the air.[51] When THz waves illuminate the device surface, a portion of the incident wave is reflected at the top layer, while the remaining part propagates into the SiO_2 layer. The transmitted wave is totally reflected by the metallic ground plane after travelling through the SiO_2 layer. The escaping wave component is responsible for the absorption term $T_{12}T_{21}R_{23}e^{i2\beta}$, where $\beta = \sqrt{\varepsilon}k_0H$ represents the total propagation phase across the SiO_2 layer, k_0 is the free-space wave number, and H is the dielectric thickness.[52] The total reflection coefficient is given by

$$r = R_{12} - T_{12}T_{21}R_{23}e^{i2\beta} + T_{12}R_{21}R_{23}R_{23}T_{21}e^{i4\beta} - \ldots \tag{3}$$

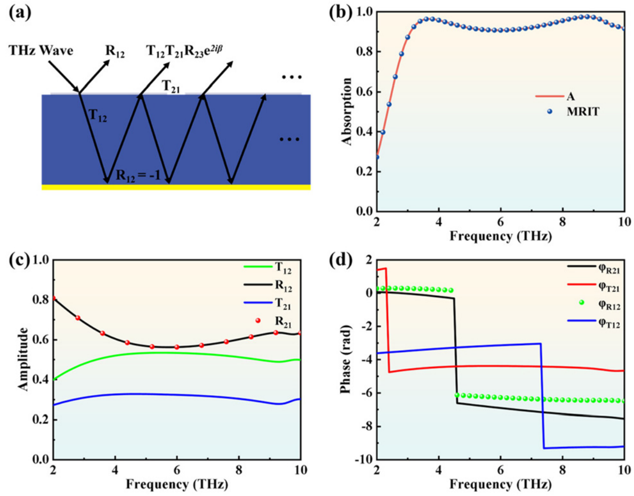

Fig. 2 (a) Schematic of multiple interference reflection theory. (b) Simulated and theoretical absorption curves of the device, showing an excellent match. (c) Amplitudes and (d) phases of the transmission and reflection coefficients obtained from the theoretical model.

After simplification, the reflection coefficient is approximated as

$$r \approx R_{12} - \frac{T_{12}T_{21}e^{i2\beta}}{1 + R_{21}e^{i2\beta}}. \tag{4}$$

Accordingly, the absorption of the absorber can be derived as

$$A_{\mathrm{MRIT}} = 1 - |r|^2. \tag{5}$$

Based on the MRIT illustrated in Fig. 2(a), the amplitudes and phases of the transmission and reflection coefficients are calculated, as shown in Fig. 2(c) and (d), respectively, from which the A_{MRIT} curve is derived, representing the theoretical absorption spectrum predicted using MRIT. The absorption spectrum predicted using MRIT exhibits excellent agreement with the simulated absorption results, thereby validating the theoretical framework.[53] It is worth noting that all simulation data shown in Fig. 2(b) are obtained under the metallic phase of VO_2 (345 K, $\sigma_{VO_2} = 2 \times 10^5\ \mathrm{S{\cdot}m^{-1}}$). Unless otherwise specified, all subsequent simulations are performed under the same conditions.

Broadband perfect absorbers operating in the THz regime possess significant practical value. Therefore, the absorption performance and underlying physical mechanisms of the absorber based on a metallic-phase VO_2 thin film are discussed in detail. Fig. 3(a) illustrates the absorptance of the proposed absorber at different frequencies. As observed, when the temperature is set to $T = 345$ K (the metallic phase of VO_2), the absorber exhibits an ultra-broadband absorption response in the THz region. High absorption efficiency is achieved over the frequency range of 3.1–10.0 THz, with an absorptance exceeding 90% across a bandwidth of approximately 6.9 THz. In addition, the absorptance at $f = 3.70$ THz and $f = 8.80$ THz exceeds 96%. The fractional bandwidth (FB) is calculated using the expression[54] $\mathrm{FB} = 2(f_{\max} - f_{\min})/(f_{\max} + f_{\min})$, where $f_{\min}$ and $f_{\max}$ denote the lower and upper cutoff frequencies corresponding to 90% absorption, respectively. The calculated FB reaches 105.34%. Furthermore, the identical absorption spectra under TE polarization (with the external electric field oriented along the x direction) and TM polarization (with the

Published on 05 March 2026. Downloaded on 5/23/2026 5:05:50 AM.

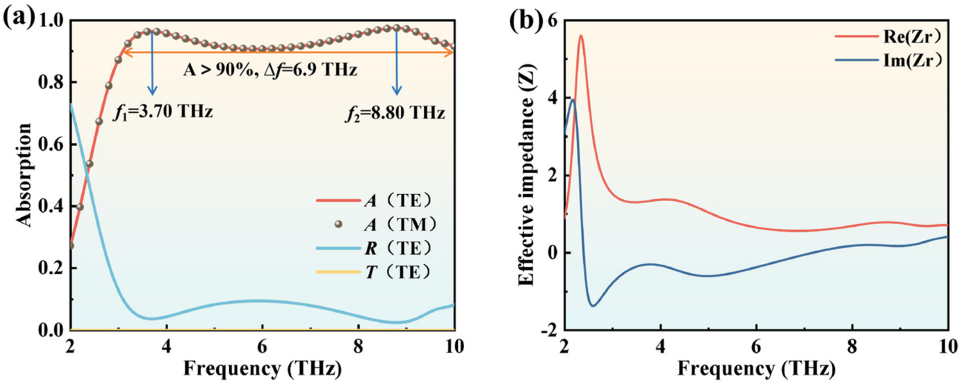

Fig. 3 (a) Absorptance, reflectance, and transmittance curves of the device under TE polarization, together with the corresponding absorptance curve under TM polarization. (b) Real part Re(Z) and imaginary part Im(Z) of the device's effective impedance Z over the 2–10 THz frequency band.

external magnetic field oriented along the x direction) confirm that the proposed absorber is polarization-insensitive.

In COMSOL simulations, the scattering parameters S_{11} and S_{21}, which are related to the reflection and transmission coefficients, can be directly obtained. According to the law of energy conservation, the absorptance $A(\omega)$ is defined as[55]

$$A(\omega) = 1 - R(\omega) - T(\omega) = 1 - |S_{11}(\omega)|^2 - |S_{21}(\omega)|^2 \quad (6)$$

Considering that the thickness of the bottom gold layer is much larger than the skin depth in the THz regime ($\delta \approx 0.25$ μm), the transmission $T(\omega)$ can be approximated as zero. Consequently, the absorptance expression is simplified as[56]

$$A(\omega) = 1 - |S_{11}(\omega)|^2 \quad (7)$$

When $R(\omega) = 0$, perfect absorption is achieved, corresponding to $A(\omega) = 1$.[57] To further elucidate the absorption mechanism, impedance matching theory is introduced. The relative impedance can be expressed as[58,59]

$$Z_r = \sqrt{\frac{(1 + S_{11}(\omega))^2 - S_{21}{}^2(\omega)}{(1 - S_{11}(\omega))^2 - S_{21}{}^2(\omega)}} \quad (8)$$

Accordingly, the absorptance can be written as

$$A(\omega) = 1 - R(\omega) = 1 - \left|\frac{Z - Z_0}{Z + Z_0}\right|^2 = 1 - \left|\frac{Z_r - 1}{Z_r + 1}\right|^2 \quad (9)$$

where Z and Z_0 represent the effective impedance of the absorber and the impedance of free space, respectively, and the normalized impedance is defined as $Z_r = Z/Z_0$. Here, μ and ε denote the relative permeability and relative permittivity of the absorber.

When the effective impedance of the absorber is well matched to that of free space, superior absorption performance can be achieved. In particular, optimal absorption occurs when the real part of the normalized impedance approaches 1 and the imaginary part approaches 0.[60] As shown in Fig. 3(b), over the entire frequency range of 3.1–10.0 THz, the real part of the normalized impedance Re(Z_r) remains close to 1, while the imaginary part Im(Z_r) stays near 0. Under these conditions, reflection is effectively suppressed and high absorptance is maintained, indicating excellent impedance matching across a broad bandwidth.[61] This matching behavior efficiently minimizes reflection losses, thereby ensuring stable and high-efficiency broadband absorption.

When variations in the ambient temperature induce a phase transition in VO_2, the electrical conductivity of vanadium dioxide changes accordingly. This variation disrupts the impedance matching between the absorber and the surrounding dielectric environment, leading to strong reflection of incident electromagnetic waves and degraded absorption performance. Similarly, when the temperature is fixed, a reduction in the thickness of the VO_2 layer increases the electromagnetic transmittance, which also results in a decrease in absorptance.

Fig. 4(a) illustrates the theoretically derived temperature-dependent electrical conductivity of VO_2. In the insulating state ($T < 313$ K), the conductivity remains lower than 200 $S \cdot m^{-1}$. Near the critical phase transition temperature of approximately 341 K, the conductivity increases sharply by nearly three orders of magnitude. As the temperature further rises above 345 K, the peak conductivity reaches 2×10^5 $S \cdot m^{-1}$. By thermally regulating the phase transition of VO_2, its electrical conductivity can be effectively tuned, thereby enabling dynamic control of electromagnetic wave interactions.[31–34] As shown in Fig. 4(b), based on the unit-cell simulation platform, the proposed device exhibits a wide dynamic modulation range of spectral absorptance, varying from nearly 0 to 0.997 through temperature tuning. At lower temperatures, owing to the low conductivity of VO_2 in its insulating phase, the device predominantly reflects incident terahertz waves. With increasing temperature, the absorption efficiency is significantly enhanced. VO_2 begins to undergo the insulator–metal transition (IMT) at around 342 K and becomes fully metallic near 353 K, at which point it enters a fully metallic state. In this regime, the enhanced conductivity facilitates stronger resonance coupling and improved local field confinement, thereby markedly improving the absorber performance within the

This journal is © The Royal Society of Chemistry 2026

Published on 05 March 2026. Downloaded on 5/23/2026 5:05:50 AM.

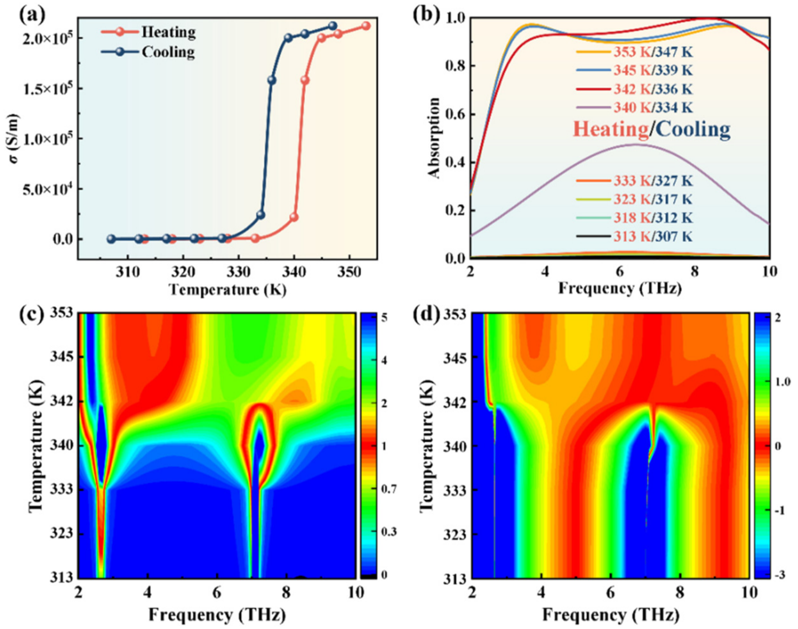

Fig. 4 (a) Temperature-driven evolution of VO_2 conductivity. (b) Variation in the absorption spectrum of the device with temperature. (c) Real part Re(Z) and (d) imaginary part Im(Z) of the effective impedance Z of the device over the 2–10 THz frequency band as functions of temperature.

target frequency range.[62–64] Subsequent analyses are performed under a conductivity of 2×10^5 S·m^{-1} to further investigate the underlying absorption mechanisms.

Optimal absorption is achieved when the real part of the normalized impedance approaches 1 and the imaginary part approaches 0. Fig. 4(c) and (d) present the frequency-dependent responses of the real and imaginary parts of the impedance over the temperature range from 313 to 353 K, covering a frequency span of 2–10 THz. As shown in Fig. 4(c), with increasing temperature, a pronounced variation in the real part of the impedance is observed near 340 K, which coincides well with the phase transition of VO_2 from the insulating to the metallic state. This abrupt phase transition leads to significant changes in the impedance, particularly in the vicinity of the transition temperature, where the real part of the impedance increases markedly, indicating a substantial modification of the electrical conductivity of VO_2. The impedance variation is most pronounced in the frequency range of approximately 4–6 THz. A similar trend is observed in Fig. 4(d). When the temperature further increases and VO_2 fully transforms into the metallic phase, the imaginary part of the impedance gradually stabilizes, exhibiting more consistent impedance characteristics. This temperature-dependent impedance modulation demonstrates that VO_2-based metamaterials enable dynamic tunability, offering promising potential for devices requiring adjustable absorption or impedance characteristics, such as terahertz sensors and modulators.

To further elucidate the underlying physical mechanisms responsible for the broadband and high-efficiency absorption of the proposed device, the electric field distributions on the surface of the VO_2 layer are calculated at frequencies corresponding to high absorptance. Specifically, the electric field intensity ($|E|$) on the VO_2 surface is evaluated at two representative high-absorption frequencies, f_1 = 3.70 THz and f_2 = 8.80 THz. As shown in Fig. 5(a) and (b), the electric field is predominantly concentrated at the edges of the four fan-shaped elements and the central pattern, exhibiting pronounced local field enhancement and effectively exciting LSPR.[65–67] This strong field confinement efficiently suppresses the escape of terahertz waves from the absorber surface, thereby enabling near-perfect absorption. The distributions of the vertical electric field component E_Z, as shown in Fig. 5(c) and (d), further reveal that the central VO_2 structure, under the coupling effect of the surrounding fan-shaped array, excites a pair of electric dipoles with identical magnitudes but opposite polarities. Consequently, the strong THz absorption is primarily governed by electric dipole resonance. At resonance, the incident THz waves are tightly confined to the surface of the VO_2 layer, significantly reducing reflection at the absorber interface and thus realizing efficient absorption.[68,69] In addition, it is noteworthy that electric dipoles with opposite polarities are also formed on both sides of the slits between the surrounding fan-shaped array and the central pattern, indicating that the slit configuration plays an important role in achieving broadband absorption.[70]

To gain deeper insight into the absorption mechanisms over the entire frequency range, multipole decomposition is employed to analyze the physical origins of electromagnetic resonances and scattering phenomena. Through the decomposition of the electric field into multipole components, the generation principle is explored.[71] Certain multipoles may be computed from the displacement current density induced across the metamaterial:[72,73]

Published on 05 March 2026. Downloaded on 5/23/2026 5:05:50 AM.

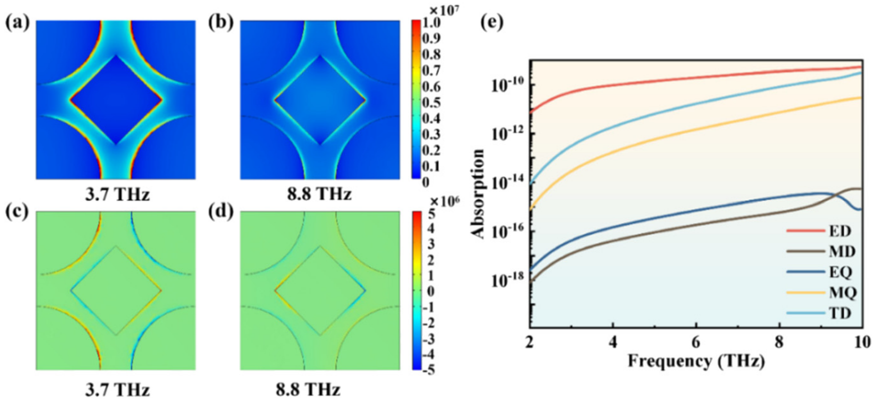

Fig. 5 Electric field distributions of the device at two representative absorption peak frequencies under TE polarization when the conductivity of VO_2 is 2×10^5 S m^{-1}. (a) and (b) Electric-field magnitudes $|E|$ at f_1 = 3.70 THz and f_2 = 8.80 THz, respectively. (c) and (d) Corresponding vertical components E_Z at these frequencies. (e) Multipolar decomposition analysis.

Electric dipole (ED):

$$I_{\mathrm{ED}} = \frac{2\omega^4}{3c^2}\left|\frac{\int j d^3 r}{i\omega}\right|^2 \tag{10}$$

Magnetic dipole (MD):

$$I_{\mathrm{MD}} = \frac{2\omega^4}{3c^2}\left|\frac{\int (r \times j) d^3 r}{2c}\right|^2 \tag{11}$$

Toroidal dipole (TD):

$$I_{\mathrm{TD}} = \frac{2\omega^6}{3c^5}\left|\frac{\int [(r \cdot j)r - 2r^2 j] d^3 r}{10c}\right|^2 \tag{12}$$

Electric quadrupole (EQ):[74]

$$I_{\mathrm{EQ}} = \frac{\omega^6}{5c^5}\left|\frac{\int [r_\beta j_\alpha + r_\alpha j_\beta) - \frac{2}{3}(r \cdot j)] d^3 r}{i\omega}\right|^2 \tag{13}$$

Magnetic quadrupole (MQ):[75]

$$I_{\mathrm{MQ}} = \frac{\omega^6}{40c^5}\sum\left|\frac{\int [(r \times j)_\alpha r_\beta + ((r \times j)_\beta r_\alpha)] d^3 r}{3c}\right|^2 \tag{14}$$

In the above equations, j denotes the resultant current density, c represents the speed of light, and ω is the angular frequency of the incident wave, while α and β correspond to the x and y axis directions, respectively. The results of the multipole decomposition calculated over the frequency range of 2–10 THz are presented in Fig. 5(e). It is evident that the electric dipole (ED) contribution to the total far-field scattering power exceeds the contributions of other multipole components by several orders of magnitude, indicating its dominant role in the absorption behavior of the device.[76] It is worth noting that at the frequency f_2, the contributions of both the electric dipole (ED) and the magnetic dipole (MD) are stronger than those at f_1. This observation suggests that multipole resonances at higher frequencies, particularly ED and MD resonances, are more pronounced, leading to enhanced absorption. This effect explains why the absorptance at f_2 is slightly higher than that at f_1. Therefore, the broadband and high-efficiency absorption of the proposed device can be attributed to a synergistic multipole coupling mechanism dominated by the electric dipole resonance, with auxiliary contributions from toroidal dipole and magnetic dipole resonances.

By optimizing the key geometric parameters within the unit cell of the metamaterial absorber, the effective impedance and resonant behavior can be precisely modulated.[77] Moreover, analyzing the tolerance of these parameters provides important guidance for practical fabrication. Accordingly, the influences of the structural parameters H, R, and D on the absorption performance are systematically investigated, as shown in Fig. 6. As illustrated in Fig. 6(a), when the dielectric thickness H varies within the range of 6.7–8.7 μm, the absorber maintains high absorptance over the frequency range of 3.0–9.5 THz, with the absorption approaching saturation in the mid-frequency region, indicating favorable impedance matching under these conditions. When H is increased to 8.7 μm, an increase in the thickness of the dielectric layer induces a redshift in the absorption spectrum. Although the high-frequency absorption is slightly reduced, the broadband and high-efficiency absorption performance is still preserved. The reduction in high-frequency absorption can be mainly attributed to the excessive phase delay introduced by an overly thick dielectric layer, which disrupts the constructive interference condition and weakens the coupling between local field enhancement and the resonant structure.[78] As shown in Fig. 6(b), increasing the fan-shaped radius R slightly enhances absorption in both the low and high frequency regions, while the absorptance in the mid frequency range decreases marginally. As a result, the absorption spectrum becomes less concentrated around the central frequency, leading to an overall broadening of the absorption bandwidth. The reduced slit width enhances the electric field coupling between adjacent patterns and strengthens local field confinement, thereby expanding the absorption bandwidth.[79] Similarly, as depicted in Fig. 6(c), the absorption bandwidth increases steadily with increasing values of both the fan-shaped radius R and the side

This journal is © The Royal Society of Chemistry 2026

Published on 05 March 2026. Downloaded on 5/23/2026 5:05:50 AM.

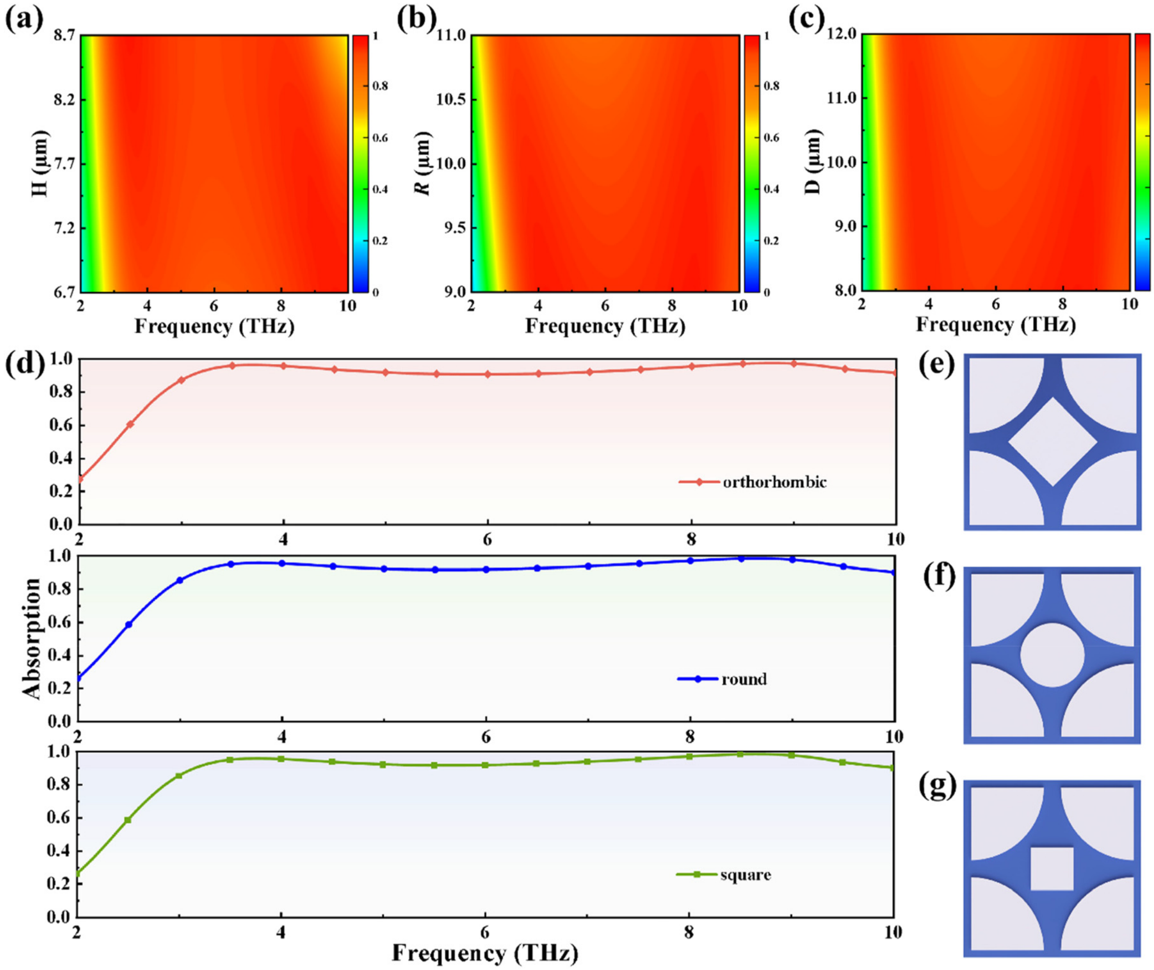

Fig. 6 Absorption spectra of the device with different internal VO_2 geometries and corresponding top-layer patterns, and the influence of the geometric parameters on absorption performance when the conductivity of VO_2 is 2×10^5 S m^{-1}. (a) Center-square side length *D*. (b) Sector radius *R*. (c) SiO_2 dielectric-layer thickness *H*. (d) The absorption spectra of the device with rhombus-, round-, and square-shaped internal VO_2 inclusions. (e) Top-layer pattern with an internal rhombus-shaped VO_2. (f) Top-layer pattern with an internal round VO_2. (g) Top-layer pattern with an internal square VO_2.

length *D* of the central diamond structure. This behavior arises because both parameters directly reduce the slit spacing, which leads to enhanced electromagnetic coupling and a corresponding increase in absorption bandwidth.[80] In summary, the proposed absorber design exhibits excellent fabrication tolerance and enables cost-effective manufacturing without compromising its broadband absorption performance.

By varying the geometry of the top-layer VO_2 pattern, the characteristics of the proposed absorber can be further elucidated. As illustrated in Fig. 6(d), the absorption spectra of absorbers with rhombus, round, and square VO_2 patterns on the top layer are presented, with the corresponding geometries illustrated in Fig. 6(e)–7(g), respectively. As the top-layer VO_2 pattern transitions from a rhombus to a round and then to a square, only minor variations in the absorption performance are observed. This behavior can be attributed to the persistent presence of the slit structure, which ensures that the majority of the electromagnetic field remains strongly localized within the slits. These results demonstrate that the proposed design exhibits excellent fabrication tolerance, highlighting its robustness against variations in the top-layer geometry.

Considering the diversity of incident angles and polarization states in practical applications, it is essential for the device to exhibit wide-angle absorption and polarization stability. Therefore, detailed numerical simulations are performed using COMSOL Multiphysics to investigate the response characteristics of the proposed absorber under TE and TM polarizations as the incident angle increases from 0° to 60°. At an incidence angle of 40°, the absorptance above 90% spans 3.6–10.0 THz under TM polarization, while at 50° it spans 3.8–10.0 THz. Under TE polarization, the corresponding 90% absorption ranges are 3.3–10.0 THz and 3.2–10.0 THz, respectively. As depicted in Fig. 7(a), under TM polarization, the absorber maintains high absorption efficiency over the frequency range of 3.0–10.0 THz. When the incident angle

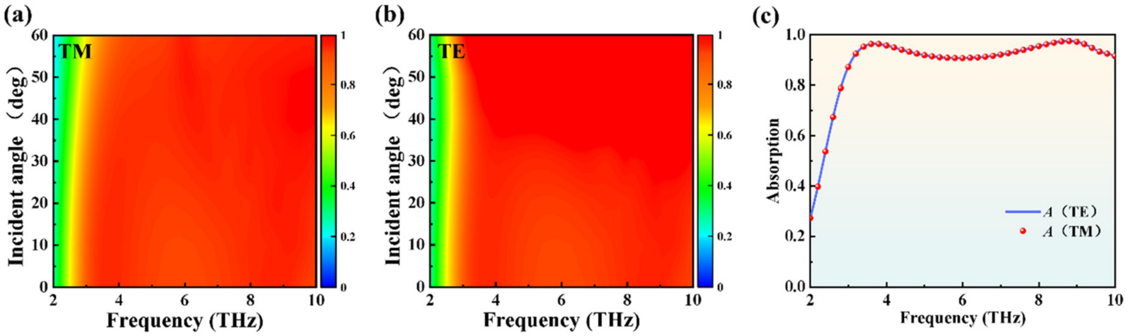

Fig. 7 Angular response of the device with the conductivity of VO_2 being 2×10^5 S m^{-1} at different incidence angles in (a) TE mode and (b) TM mode. (c) Absorption spectra under normal incidence with TE and TM polarizations.

Published on 05 March 2026. Downloaded on 5/23/2026 5:05:50 AM.

increases to 40°, the absorption bandwidth decreases slightly and is further reduced at 50°. Although the absorptance gradually decreases with increasing incident angle, the absorption bandwidth remains sufficiently broad, demonstrating excellent broadband absorption capability and strong angular stability. This behavior can be primarily attributed to the presence of an electric field component perpendicular to the surface under TM polarization, which makes the resonant response more sensitive to variations in reflection paths and phase accumulation, thereby reducing the coupling efficiency.[81] As depicted in Fig. 7(b), under TE polarization, the absorber also maintains high absorption efficiency across the 3.0–10.0 THz frequency range. As the incident angle varies from 0° to 60°, the absorptance consistently remains above 90%, highlighting the outstanding broadband performance and angular robustness of the device. This result indicates that the structure effectively couples to the electric field component parallel to the surface. Moreover, the centrosymmetric geometry and continuous edge design of the absorber play a crucial role in suppressing phase mismatch, thereby preserving stable resonant conditions and efficient impedance matching over a wide range of incident angles.[82] To further evaluate the polarization-dependent response, Fig. 7(c) presents a direct comparison of the absorption spectra under TE and TM polarizations at normal incidence. The nearly identical absorption behavior observed for both polarization states over the entire operating bandwidth confirms the polarization insensitivity of the proposed absorber, which can be attributed to its symmetric structural configuration.

To more clearly demonstrate the overall performance of the proposed THz absorber, Table 1 summarizes and shows a comparison of representative broadband absorbers reported in recent years.[83–89] The comparison covers key metrics including principal material systems, the absorption range, the tunability level, absorber thickness, fractional bandwidth, fabrication tolerance, and the number of absorber layers, which collectively reflect both electromagnetic performance and practical manufacturability. The results indicate that the proposed absorber offers competitive and, in several aspects, superior comprehensive performance in terms of broadband absorption, compactness, and fabrication friendliness. (1) Broadband absorption and fractional bandwidth: compared with previously reported broadband absorbers, the proposed design maintains continuous high absorptance (>90%) over a wide frequency range of 3.1–10.0 THz, corresponding to an effective absorption bandwidth of 6.9 THz. Meanwhile, an ultra-large fractional bandwidth of 105.34% is achieved, demonstrating excellent absorption continuity and spectral stability across the operating band. (2) Compact thickness and structural simplicity: as listed in Table 1, the proposed absorber achieves the above ultra-broadband response with a compact total thickness of 9.7 μm and only three functional layers (a simple MDM stack). Compared with multilayer or hybrid designs that require more layers and increased structural complexity, this

Table 1 Performance comparison of various terahertz absorbers

Principal material	Absorber thickness (μm)	Absorption range (THz)	Tunability range (%)	Fabrication tolerance	Fractional bandwidth (%)	Number of absorber layers	Ref.
Au and VO_2	19.5	3.93–9.25	>90%	High	80.72%	4	83
Au and VO_2	9.5	3.55–9.55	>90%	High	94.81%	3	84
Au, graphene and DSM	19.5	7.67–9.17	>80%	Low	17.76%	4	85
Au and VO_2	10.7	3.90–9.30	>90%	Low	81.82%	6	86
Au, graphene, TOPAS and VO_2	13.8	6.45–11.53	>95%	Low	56.51%	4	87
Au and VO_2	9.5	3.40–10.0	>90%	High	98.50%	3	88
Ag, PTFE, graphene and VO_2	19.0	3.40–7.31	>90%	Low	73.02%	4	86
Au, graphene and VO_2	7.5	3.76–11.65	>90%	High	102.40%	3	89
Au and VO_2	9.7	3.10–10.0	>90%	High	105.34%	3	This work

This journal is © The Royal Society of Chemistry 2026

Published on 05 March 2026. Downloaded on 5/23/2026 5:05:50 AM.

simplified configuration reduces fabrication difficulty and improves the feasibility for practical implementation. (3) Fabrication tolerance and robustness: in addition to the reduced layer number, the proposed absorber exhibits high fabrication tolerance, as confirmed by parametric perturbation studies on key geometric dimensions as well as variations in the top-layer VO_2 pattern shape. Only minor variations in absorptance are observed under reasonable dimensional deviations, further supporting the robustness and manufacturability of the proposed structure. Moreover, the absorber preserves polarization-insensitive and angularly stable broadband absorption, reinforcing its reliability under diverse incidence conditions.

4. Conclusions

In this work, an ultra-broadband and thermally tunable terahertz metamaterial absorber with high fabrication tolerance is demonstrated based on a VO_2-based MDM configuration. When VO_2 is in the metallic phase, the proposed absorber exhibits absorptance exceeding 90% over a wide frequency range from 3.1 to 10.0 THz, corresponding to an ultra-large fractional bandwidth of 105.34%, while maintaining polarization insensitivity and wide-angle stability. The broadband absorption mechanism is systematically clarified through impedance matching analysis, electric-field distributions, and multipole decomposition, revealing that the absorption is dominated by electric dipole resonance with auxiliary contributions from toroidal and magnetic dipole resonances. In addition, thermal modulation of the VO_2 phase transition enables dynamic tuning of the absorption response, and comprehensive parametric and structural-shape analyses verify the excellent fabrication tolerance of the design. From a fabrication standpoint, the proposed $Au/SiO_2/VO_2$ trilayer stack is compatible with conventional thin-film processes (sputtering and PECVD) and a single-step top-pattern definition. Importantly, the demonstrated robustness against geometric variations further supports the feasibility for practical fabrication. Owing to its broadband performance, tunability, angular robustness, and fabrication-friendly characteristics, the proposed absorber provides a promising platform for practical terahertz applications such as sensing, modulation, and electromagnetic energy management.

Conflicts of interest

There are no conflicts to declare.

Data availability

The data are available from the corresponding author on reasonable request.

Acknowledgements

This work was supported in part by the Natural Science Foundation of China under Grant 11604252; in part by the Science and Technology Program of Shaanxi Province under Grant 2023-JC-YB-552; in part by the Opening Project of Key Laboratory of Optoelectronic Chemical Materials and Devices, Ministry of Education, Jianghan University under Grant JDGD-202310; in part by the Program of State Key Laboratory of Infrared Physics under Grant M202001; and in part by the Program of the Key Laboratory of Artificial Microstructure, Ministry of Education under Grant 13022019af002.

References

1 S. Rane, S. Prabhu and D. R. Chowdhury, *Opto-Electron. Sci.*, 2024, **3**, 230049.

2 L. L. Xu, D. X. Yan, X. J. Li, L. Zhang and J. N. Li, *Phys. Scr.*, 2024, **99**(4), 045525.

3 Z. Y. Jin, M. S. Liu, S. B. Cheng, Z. Yi, J. Q. Wang and B. X. Li, *Mod. Phys. Lett. B*, 2026, **40**(6), 2650017.

4 X. Y. Tang and F. Chen, *Micro Nanostruct.*, 2025, **207**, 208265.

5 Z. Y. Chen, M. S. Liu, S. B. Cheng, J. Q. Wang, Y. G. Yi, B. X. Li, C. J. Tang and F. Gao, *Curr. Appl. Phys.*, 2025, **80**, 282–290.

6 Z. Wang, W. K. Pan and H. Ye, *etal.*, *Opto-Electron. Sci.*, 2025, **4**, 240024.

7 Y. X. Tian, B. Y. Dong and Y. X. Li, *etal.*, *Opto-Electron. Sci.*, 2024, **3**, 230051.

8 W. X. Li, Y. T. Yi, H. Yang, S. B. Cheng, W. X. Yang, H. F. Zhang, Z. Yi, Y. G. Yi and H. L. Li, *Commun. Theor. Phys.*, 2023, **75**, 045503.

9 Y. M. Wang, F. Fan and H. J. Zhao, *etal.*, *Opto-Electron. Adv.*, 2025, **8**, 240250.

10 Z. L. Zeng, H. F. Li, H. F. Zhang, S. B. Cheng, Y. G. Yi, Z. Yi, J. Q. Wang and J. G. Zhang, *Photonics Nanostruct. – Fundam. Appl.*, 2025, **63**, 101347.

11 Y. W. Mei, J. Q. Wang, Q. Q. Wang, M. S. Xue, J. N. He and J. Y. Yang, *Opt. Commun.*, 2026, **607**, 132938.

12 S. C. Xu, M. Tian, C. H. Li, G. F. Liu, J. H. Wang, T. T. Yan and Z. Li, *Chem. Eng. J.*, 2025, **505**, 159386.

13 H. Yang, J. Xu, M. Y. Peng, H. R. He, Y. T. Jiang, D. Yu, R. B. Jin, Y. J. Gu, Y. Q. Hu, H. G. Duan and H. Jing, *Sci. Adv.*, 2025, **11**(42), eadz5123.

14 M. J. Xu, D. X. Yan, Y. Wang, X. J. Li, L. Zhang and J. N. Li, *Front. Phys.*, 2026, **21**(4), 044201.

15 J. Li, X. G. Lu and H. Li, *etal.*, *Opto-Electron. Adv.*, 2024, **7**, 240075.

16 H. G. Wang, Z. Yi, S. B. Cheng, C. J. Tang, F. Gao and B. X. Li, *Infrared Phys. Technol.*, 2026, **152**, 106218.

17 Z. Li, H. Yang, L. B. Jia, Z. Yi, S. B. Cheng, C. J. Tang, J. Deng and B. X. Li, *Phys. Status Solidi RRL*, 2025, **19**(10), 2500194.

Published on 05 March 2026. Downloaded on 5/23/2026 5:05:50 AM.

18 N. I. Landy, S. Sajuyigbe, J. J. Mock, D. R. Smith and W. J. Padilla, *Phys. Rev. Lett.*, 2008, **100**, 207402.

19 J. Q. Yang, Q. Lin, L. L. Wang and G. D. Liu, *Phys. Scr.*, 2025, **100**, 065551.

20 H. Y. Wang, R. Ma, G. D. Liu, L. L. Wang and Q. Lin, *Opt. Express*, 2023, **31**(20), 32422.

21 Z. Li, Q. J. Song, L. B. Jia, Z. Yi, S. B. Cheng, J. Q. Wang and B. X. Li, *Opt. Commun.*, 2025, **583**, 131768.

22 Q. H. Wang, X. W. Ju, Q. Lin and J. Y. Hu, *Opt. Commun.*, 2025, **577**, 131448.

23 Z. C. Ma, B. X. Li, L. L. Zeng, Y. Fan, Y. W. Deng, G. X. Zhong, Z. Z. Shao and H. Q. Xu, *Phys. E*, 2025, **173**, 116334.

24 Q. B. Yang, L. L. Zeng, M. H. Wang, B. W. Guo, Y. F. Deng, S. X. Xu and B. X. Li, *Phys. E*, 2025, **177**, 116456.

25 X. Huang, Q. Lin, S. X. Xia, X. Zhai and G. D. Liu, *Opt. Express*, 2025, **33**(23), 48707–48716.

26 H. M. Zhao, X. Y. Wang, Q. Lin, X. Zhai and G. D. Liu, *J. Phys. D: Appl. Phys.*, 2026, **59**, 025105.

27 J. Wang, M. S. Liu, H. Yang, Z. Yi, C. J. Tang, F. Gao, J. Q. Wang and B. X. Li, *Micro Nanostruct.*, 2025, **208**, 208353.

28 Z. Ai, H. Yang, M. S. Liu, S. B. Cheng, J. Q. Wang, C. J. Tang, F. Gao and B. X. Li, *Phys. E*, 2025, **173**, 116327.

29 G. W. Zhou, T. Y. Sun, Q. J. Song, W. Zhang, Z. Yi and Y. G. Yi, *Surf. Interfaces*, 2025, **72**, 107289.

30 R. Y. Zheng, Y. T. Yi, Q. J. Song, Z. Yi, Y. G. Yi, S. B. Cheng, J. G. Zhang, C. J. Tang, T. Y. Sun and Q. D. Zeng, *Materials*, 2024, **17**, 4287.

31 T. Xu, W. M. Zhang, Q. J. Song, Z. Yi, C. Ma, S. B. Cheng, Z. Q. Hao, T. Y. Sun, P. H. Wu, C. J. Tang and Q. D. Zeng, *Surf. Interfaces*, 2024, **52**, 104868.

32 X. Ning, Q. Song, Z. Yi, J. Zhang and Y. Yi, *Nanomaterials*, 2025, **15**, 867.

33 K. Chen, Z. Wang, M. Guan, S. Cheng, H. Ma, Z. Yi and B. Li, *Photonics*, 2025, **12**, 987.

34 X. C. Liu, M. S. Liu, Y. T. Yi and Y. G. Yi, *Mod. Phys. Lett. B*, 2026, **40**(5), 2650013.

35 J. Luo, J. T. Guo, G. X. Zhao, Y. Shao, P. H. Wu, P. Chen and Z. Yi, *Coatings*, 2026, **16**(2), 211.

36 Y. R. Li, W. H. Liu, R. C. Liu, J. J. Gao, J. W. Feng, S. C. Xu, Z. Li, S. Z. Jiang and X. J. Du, *Opt. Laser Technol.*, 2023, **167**, 109825.

37 H. R. He, G. T. Cao, S. H. Zhang, H. Xu, Z. Q. Chen, Y. T. Jiang, Y. Q. Hu, H. Jing, H. G. Duan and H. Yang, *Adv. Sci.*, 2026, **13**, e21354.

38 Y. J. Cao, C. J. Wu, X. J. Li, L. Zhang, J. N. Li and D. X. Yan, *Infrared Phys. Technol.*, 2026, **153**, 106350.

39 X. M. Chen, D. X. Yan, Y. Wang, L. Zhang, S. Sun and J. N. Li, *J. Lightwave Technol.*, 2025, **43**(19), 9382–9395.

40 P. H. Wu, W. C. Zhao, L. N. Cui and P. P. Jiang, *Int. J. Therm. Sci.*, 2026, **223**, 110620.

41 Y. Jo, H. Park and H. Yoon, *etal.*, *Opto-Electron. Adv.*, 2024, **7**, 240122.

42 H. Zhang, Q. Q. Wang, J. Y. Yang, Y. W. Mei and J. Q. Wang, *Opt. Commun.*, 2025, **596**, 132581.

43 J. H. Du, X. F. Sun, S. F. Wang, Z. Yi, G. R. Liu and H. Yang, *Appl. Surf. Sci.*, 2026, **719**, 165024.

44 M. X. Luo, Y. Y. Xia, Y. K. Zhang, X. F. Sun, Z. Yi, S. F. Wang, G. R. Liu and H. Yang, *Surf. Interfaces*, 2025, **77**, 108060.

45 Q. S. Wang, Y. Fang and Y. Meng, *etal.*, *Opto-Electron. Adv.*, 2024, **7**, 240112.

46 C. C. Zhao, D. X. Yan, X. J. Li, Y. Wang, L. Zhang and J. N. Li, *Opt. Commun.*, 2025, **575**, 131313.

47 A. X. Zhou, M. S. Liu, Z. Yi, C. J. Tang, J. Deng and B. X. Li, *Phys. Status Solidi RRL*, 2026, **20**(1), e202500324.

48 K. An, M. S. Liu, H. Yang, Z. Yi, C. J. Tang, J. Deng, J. Q. Wang and B. X. Li, *Phys. E*, 2026, **175**, 116377.

49 J. Wang, M. S. Liu, H. Yang, Z. Yi, C. J. Tang, J. Deng, J. Q. Wang and B. X. Li, *Opt. Commun.*, 2025, **596**, 132415.

50 Z. Ai, Y. T. Yi, H. Yang, M. S. Liu, Y. G. Yi, C. J. Tang and F. Gao, *Phys. Lett. A*, 2025, **556**, 130827.

51 Y. Yuan, H. F. Liu, M. S. Liu, W. B. Zhang, X. H. Li and S. B. Cheng, *Phys. Lett. A*, 2025, **556**, 130832.

52 H. F. Liu, J. J. Li, H. Yang, J. Q. Wang, B. X. Li, H. Zhang and Y. G. Yi, *Photonics*, 2025, **12**(5), 443.

53 Z. Ai, H. Liu, S. Cheng, H. Zhang, Z. Yi, Q. Zeng, P. Wu, J. Zhang, C. Tang and Z. Hao, *J. Phys. D:Appl. Phys.*, 2025, **58**, 185305.

54 Z. T. Li, S. B. Cheng, H. F. Zhang, W. X. Yang, Z. Yi, Y. G. Yi, J. Q. Wang, S. Ahmad and R. Raza, *Phys. Lett. A*, 2025, **534**, 130262.

55 R. Qi, X. F. Sun, S. F. Wang, Z. Yi, G. R. Liu and H. Yang, *Mater. Today Energy*, 2025, **54**, 102142.

56 X. F. Sun, Z. Yi, S. F. Wang, G. R. Liu, X. X. Wang and H. Yang, *Sep. Purif. Technol.*, 2026, **385**, 136365.

57 Y. M. Wang, J. Q. Zhang, X. F. Sun, Z. Yi, S. F. Wang, G. R. Liu, Z. S. Pu and H. Yang, *Mater. Res. Bull.*, 2026, **197**, 113965.

58 M. X. Luo, Z. Yi, Y. Q. Li, A. Q. Yang, S. F. Wang, X. F. Sun, G. R. Liu and H. Yang, *Adv. Sustainable Syst.*, 2026, **10**, e01515.

59 X. Mu, X. F. Sun, Z. Yi, S. F. Wang, B. Kakavandi, G. R. Liu and H. Yang, *Energy Environ., Mater.*, 2026, e70247.

60 M. Tian, J. S. Wei, E. G. Lv, C. H. Li, G. F. Liu, Y. Sun, W. Yang, Q. Z. Wang, C. C. Shen, C. Zhang, B. Y. Man, J. H. Wang, B. Zhao and S. C. Xu, *Chem. Eng. J.*, 2024, **498**, 155355.

61 L. Li, Z. Yi, S. B. Cheng, C. J. Tang, F. Gao and B. X. Li, *Phys. Status Solidi RRL*, 2026, e202500447.

62 J. X. Jiang, Y. T. Yi, Q. J. Song, Z. Yi, C. Ma, Q. D. Zeng, T. Y. Sun, S. B. Cheng, Y. G. Yi and M. N. Akhtar, *Phys. E*, 2025, **165**, 116123.

63 X. Ning, T. Y. Sun, Q. J. Song, Z. Yi, S. B. Cheng, J. Q. Wang, Q. D. Zeng and Y. G. Yi, *Commun. Theor. Phys.*, 2025, **77**, 095702.

64 Y. Liu, M. Liu, H. Yang, Z. Yi, H. Zhang, C. Tang, J. Deng, J. Q. Wang and B. X. Li, *Phys. Lett. A*, 2025, **552**, 130653.

65 W. X. Li, S. B. Cheng, H. F. Zhang, Z. Yi, B. Tang, C. Ma, P. H. Wu, Q. D. Zeng and R. Raza, *Commun. Theor. Phys.*, 2024, **76**, 065701.

66 Y. X. Yi, Z. Yi, Z. G. Zhou, H. Yang, J. Q. Wang, C. J. Tang, J. Deng and B. X. Li, *Phys. B*, 2025, **715**, 417549.

This journal is © The Royal Society of Chemistry 2026

Published on 05 March 2026. Downloaded on 5/23/2026 5:05:50 AM.

67 Z. T. Li, X. Li, G. D. Liu, L. L. Wang and Q. Lin, *Opt. Express*, 2023, **31**(19), 30458.

68 G. F. Liu, Z. X. Wang, W. Sun, X. H. Lin, R. Wang, C. H. Li, L. Zong, Z. L. Fu, H. P. Liu and S. C. Xu, *Chem. Eng. J.*, 2023, **452**, 139504.

69 Z. H. Zhu, D. X. Yan, L. L. Xu, X. J. Li, L. Zhang and J. N. Li, *IEEE J. Sel. Top. Quantum Electron.*, 2024, **30**(6), 4300610.

70 W. Li, S. Cheng, Z. Yi, H. Zhang, Q. Song, Z. Hao, T. Y. Sun, P. H. Wu, Q. D. Zeng and R. Raza, *Appl. Phys. Lett.*, 2025, **126**, 033503.

71 S. B. Cheng, W. X. Li, H. F. Zhang, M. N. Akhtar, Z. Yi, Q. D. Zeng, C. Ma, T. Y. Sun, P. H. Wu and S. Ahmad, *Opt. Commun.*, 2024, **569**, 130816.

72 Z. Y. Chen, S. B. Cheng, H. F. Zhang, Z. Yi, B. Tang, J. Chen, J. G. Zhang and C. J. Tang, *Phys. Lett. A*, 2024, **517**, 129675.

73 S. H. Liu and F. Chen, *Phys. B*, 2025, **715**, 417638.

74 B. W. Liu and F. Chen, *Phys. B*, 2025, **714**, 417423.

75 L. Y. Li and F. Chen, *Phys. Lett. A*, 2025, **544**, 130489.

76 Y. X. Yi, W. L. Zhu and Z. Yi, *etal.*, *Opto-Electron. Sci.*, 2026, **5**, 250027.

77 Y. X. Zeng, B. X. Li, L. L. Zeng, G. X. Zhong, Z. Z. Shao, H. Q. Xu, M. L. Liu, Z. G. Chen and C. J. Dai, *Eur. Phys. J. Plus*, 2025, **140**, 416.

78 Y. Fan, B. X. Li, L. L. Zeng, Z. C. Ma, Y. W. Deng and Z. Z. Shao, *Phys. Scr.*, 2025, **100**, 055905.

79 C. Tuo, J. Zhu, Z. Yi, B. X. Li and S. B. Cheng, *Opt. Commun.*, 2026, **599**, 132650.

80 R. Ma, L. G. Zhang, Y. Zeng, G. D. Liu, L. L. Wang and Q. Lin, *Opt. Express*, 2023, **31**(4), 482723.

81 L. Wang, Q. Lin, L. L. Wang and G. D. Liu, *J. Appl. Phys.*, 2025, **137**(23), 234303.

82 Q. H. Wang, X. W. Ju, C. Yang, Y. Zhang and J. Y. Hu, *Phys. Scr.*, 2025, **100**(3), 035538.

83 L. Shao, H. Yang, Z. Yi, J. Wang, C. Tang, J. Deng and B. Li, *Phys. B*, 2025, **714**, 417427.

84 G. Zou, T. Liu, C. Wang, C. Luo, Z. Qin, J. Ji and Z. Yi, *Dalton Trans.*, 2025, **54**, 10898–10906.

85 J. Zhou, X. Sun, J. Xu, S. Wu, K. Jin, Y. Tang, Z. Yi and Y. Yi, *Molecules*, 2025, **30**, 999.

86 N. Liu, Z. Cui, S. Zhang and L. Wang, *Solid State Commun.*, 2025, **399**, 115884.

87 J. Xiong, C. Li, D. Wang, S. Gao, Y. Che, G. Wu and M. Guo, *J. Mater. Chem. C*, 2025, **13**, 4160–4169.

88 X. Zhou, T. Liu, C. Wang, Z. Qin, M. Zhao, H. Shi, T. Yu and Z. Yi, *Int. J. Therm. Sci.*, 2026, **220**, 110402.

89 Z. Chen, S. Wang, H. Chen, X. Wu, S. Pu and B. Dai, *Dalton Trans.*, 2026, **55**, 507–521.

This journal is © The Royal Society of Chemistry 2026